STRUCTURAL CHARACTERIZATION OF A TRITRUSS MODULE

by

Lauren M. Simmons
B.S. May 2017, Virginia Tech

A Thesis Submitted to the Faculty of
Old Dominion University in Partial Fulfillment of the
Requirements for the Degree of

MASTER OF SCIENCE

MECHANICAL ENGINEERING

OLD DOMINION UNIVERSITY
May 2024

Approved by:

Gene Hou (Director)

Miltos Kotinis (Member)

Cyrus Kosztowny (Member)

ABSTRACT

STRUCTURAL CHARACTERIZATION OF A TRITRUSS MODULE

Lauren M. Simmons
Old Dominion University, 2024
Director: Dr. Gene Hou

The TriTruss is a novel structural module developed by researchers at NASA Langley Research Center (LaRC) that can be used in space to assemble large support structures for a variety of applications. One such application is the metering truss or primary mirror backbone support structure of an In-Space Assembled Telescope (iSAT). For the iSAT application, the TriTruss will be supporting mirror segments, payloads, and instruments, all of which require the TriTruss to have a high stiffness. Structural characterization from testing and analysis is needed to ensure the integrity of the struts that make up a TriTruss module is maintained when subjected to loads representative of the application. The test setup and loads applied to the TriTruss module as well as the analytical methods used to predict the response of the structure under conditions representative of those implemented during testing will be discussed. Also, the results obtained from testing and analysis will be summarized. The goal for the characterization study was to achieve a correlation within 10% between the test data and the analysis. Overall, the correlation varied for the struts with a few struts still having a larger error margin after further studies were conducted to improve the correlation through additional analysis.

DEDICATION

I dedicate this thesis to my uncle, Kevin Paddeu, who was tragically taken from my family in 2023. He was a selfless person and a very loving uncle who would be very proud of this achievement of completing a Master's degree, just how he was in all of my other accomplishments in my young life. I think about him all the time and miss him everyday.

ACKNOWLEDGMENTS

I would like to thank Dr. Cyrus Kosztowny for being an outstanding mentor throughout my master's degree. Dr. Kosztowny has been an essential part of my development at NASA by mentoring me in finite element analysis and challenging me to improve my critical thinking skills. I am supremely grateful for his time and effort to provide mentorship, technical guidance, serving on my advisory committee, and bolstering the content presented in this thesis. I would also like to acknowledge Ms. Judith Watson for all of her mentorship regarding test set-up, execution, and test result discussions. Thank you to those who have helped me thrive in my current position of a Research Engineer in the Structural Mechanics and Concepts Branch at NASA Langley Research Center while pursuing this degree. Thank you to my current supervisors, Dr. Sandra Walker, Dr. Adam Przekop, and Dr. Christopher Wohl, for their encouragement and support of my pursuit of this degree. Thank you to my project leadership, Dr. Olive Stohlman and Jim Neilan, for enabling and supporting the research described in this thesis. To that end, I am grateful for research funding support from the NASA Precision Assembled Space Structures (PASS) project. I am also grateful to the NASA Langley Research Center Advanced Degree Program, led by Phil Kandel, for funding my degree. Furthermore, thank you to Jim Plant, Michael Scott, and, particularly, Clarence Stanfield for all the test support outlined in this thesis and also Kyongchan Song for initial analysis support. I also would like to thank Professors Gene Hou and Miltos Kotinis for their time and commitment in serving on my advisory committee. Thank you to my parents and family for their encouragement and support throughout my life. Lastly, thank you to my husband, Ben, for all his support during my graduate studies and all my other pursuits.

NOMENCLATURE

A	Cross-sectional area
a	Length of face triangle strut
d_s	Diameter of strut
E	Young's modulus
e	Applied load eccentricity
H	TriTruss module depth
I	Area moment of inertia
L_b	Length of batten member
L_c	Length of central triangle strut
l	Strut length
P	Axial compression load on strut
P_e	Euler buckling load of strut
q	Ratio of axial compression load to Euler buckling load
w	Lateral displacement of strut
w_0	Initial imperfection of strut
y	Perpendicular distance from the neutral axis to a point on the section
δ	Total lateral displacement
ε_b	Strain at bottom of strut
ε_t	Strain at top of strut
μ	Magnitude of strut initial imperfection at strut midlength
σ_b	Stress at bottom of strut
σ_t	Stress at top of strut

TABLE OF CONTENTS

LIST OF TABLES

LIST OF FIGURES

Figure Page

CHAPTER 1

INTRODUCTION

From the 1970s through the early 1990s, NASA Langley Research Center (LaRC) led studies pertaining to the design and construction of large space structures in Low Earth Orbit (LEO) using extravehicular activity (EVA) astronaut construction methods [1]. Design and fabrication of a 4-m diameter, doubly curved, tetrahedral support truss incorporated joints that were specifically designed for on-orbit astronaut assembly was part of the NASA Precision Segemented Reflector (PSR) program. Initial static and vibration tests were shown to be repeatable and generally had good agreement with linear finite element predictions [2, 3]. Then, larger segmented reflectors (>10-m diameter) were considered which would require the support truss to consist of longer struts, creating a stiffer truss (due to its increased depth). Detailed procedures for astronaut assembly of these large reflectors is outlined in Ref. [4]. Since space science and earth science communities require larger space systems with apertures >15 m [5], this can create more challenges for astronauts in EVA to assemble complex structures; therefore, robotic techniques for assembly would be the preferred method with a suitable structural concept [6–8], i.e. modular systems.

Space operations are beginning to leverage modular systems and repeated robotic visits to "Persistent Assets" (PA) enabling asset maintenance, repair, and enhancement. A "Persistent Asset" is defined as any near zero-gravity (zero-g) or planetary surface system that benefits from multiple visits [9]. These visits can be used for assembly, servicing, repairs, reconfiguration, and upgrades [10–15]. A key attribute when developing such systems is to design them to be modular and assemblable. The efficiency and robustness of on-orbit assembly operations can be maximized

by designing modular structures, such as the TriTruss [16], and their associated connectors for robotic assembly. One example of a PA that is currently being considered is the In-Space Assembled Telescope (iSAT) shown in Fig. 1.

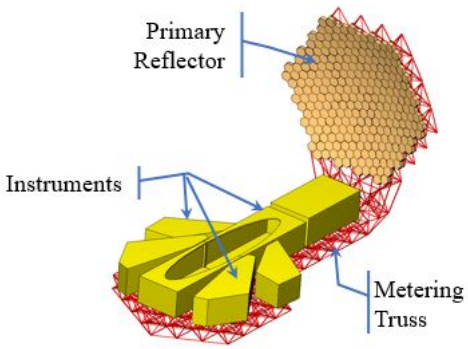

Figure 1. Large In-Space Assembled Telescope [16].

A study was conducted in 2019 [17, 18] that determined the feasibility of designing the iSAT. The study concluded that in order to achieve large apertures (>15-m diameter primary aperture), robotic in-space assembly of modular components was necessary. The study also concluded that the foundational structure for the telescope, consisting of the metering truss and the primary mirror support truss, should be assembled from modular truss elements that could be packaged prior to launch, deployed on-orbit, and robotically assembled into the final configuration. The metering truss and primary mirror support truss structures are illustrated in Fig. 2a. Although a specific truss design was not selected during the study [17, 18], the iSAT structures team baselined the modular TriTruss system for the telescope foundational structure [19], consisting of the metering truss and primary mirror support truss.

The TriTruss [16], as shown in Fig. 2b, was developed by researchers at NASA LaRC for sys-

tems with triangular or hexagonal topologies that are flat or curved, such as telescopes and other platforms. The struts of the TriTruss form equilateral triangles at the top, middle, and bottom sections. The sides of the top triangle are shorter than the bottom by 0.1 m when used to support curved surfaces such as telescope primary mirror support structures. The TriTruss has many innovative attributes including design versatility, compact packaging, robotically actuated deployment, and multiple locations for payload attachment. The TriTruss concept was first introduced in Ref. [16] where the details of its design parameters and structural configuration were described.

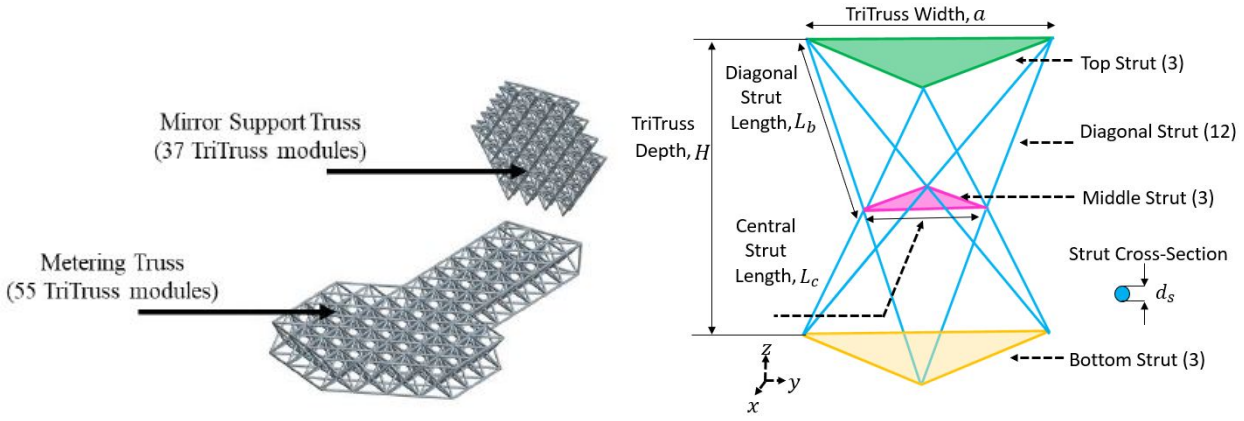

(a) Foundational support structure of an iSAT (b) Geometry and parameters of a TriTruss module

Figure 2. The foundational truss structure of an iSAT assembled from individual TriTruss modules [19].

In Ref. [16], many different mission applications for the TriTruss are discussed, including a 20-m diameter space telescope and a beam-type platform that can be used to host payloads and instruments. The geometry and various design variables for the TriTruss are also described. The TriTruss module geometry consists of top- and bottom-face equilateral triangles (strut length, a) with an equilateral central triangle (strut length, $a/2$) located halfway between the two faces. Core

struts with length, L_b, (that depend on truss depth, H) connect the central triangle with the face triangles [19]. Bonded joints were used to connect struts to joints to form the TriTruss.

Since only an approximate elastic modulus was provided for the TriTruss struts by the manufacturer of the struts, testing was performed to obtain the tensile and compressive equivalent elastic modulus to provide more accurate data for conducting the analysis. The elastic modulus test set-up and results for a TriTruss strut are described in Chapter 2. A larger space telescope requires larger instruments that must meet stiffness requirements; therefore, a characterization study is needed of the TriTruss module to investigate whether it will meet the stiffness requirements. Since the TriTruss is currently at a low technology readiness level (TRL), initial testing and analysis of the structure is needed for the TriTruss to be considered in the assembly of a metering truss and primary mirror support truss for an iSAT. The purpose of this thesis was to ascertain, for the first time, the ability to measure first generation TriTruss structural response and accurately reproduce that behavior with an analytical model, establishing a framework for prediction by analysis and design tailoring. The TriTruss module characterization test setup and description of the finite element model are discussed in Chapter 3. The results of the test, analysis, and a comparison of strain values computed from each are given in Chapter 4. The goal is to achieve a correlation within 10% between the test data and the analysis. Future work and conclusions are discussed in Chapter 5.

CHAPTER 2

ELASTIC MODULUS TEST

The purpose of this test was to establish the equivalent elastic modulus for composite struts used in a TriTruss. The equivalent elastic modulus was originally provided by the manufacturer, but disagreement between finite element analysis (FEA) results using the manufacturer-determined elastic modulus and experimental measurements in a TriTruss bond test [20] suggested that the provided elastic modulus may have been inaccurate. After further investigation, it was determined that the elastic modulus test performed by a subcontractor of the manufacturer was unsatisfactory because only one strain gage was applied to each test specimen, the test specimen appeared to be too short, and too few repeat trials were performed. The results documented in [21] were obtained by applying improved elastic modulus determination methods by conducting more test trials of longer specimens with more strain gages. A tensile and compressive equivalent elastic modulus was computed from the data obtained in this test. One strut was cut into five specimens, each one 0.3048 m in length, for the test. They were each loaded up to 6672 N in tension and 6672 N in compression at a rate of 17.79 N/s. The struts were loaded and unloaded through this range three times. An aluminum end fitting was bonded to the inside of the strut on both ends using an adhesive, the same one used in the TriTruss joints, and mounted in the test stand. The specimen was pinned using a clevis on both ends of the aluminum fittings. Three strain gages were placed on the exterior surface at the center of each strut, equally spaced around the circumference. The test set-up is shown in Fig. 3. Testing was conducted in a 50-kip MTS load frame with an inline 5-kip load cell. The inline load cell was calibrated through the MTS FlexTest 40 control system

and was set up as a load-control channel. A Micro-Measurements System 7000 data acquisition system was used for collecting load and strain gage data.

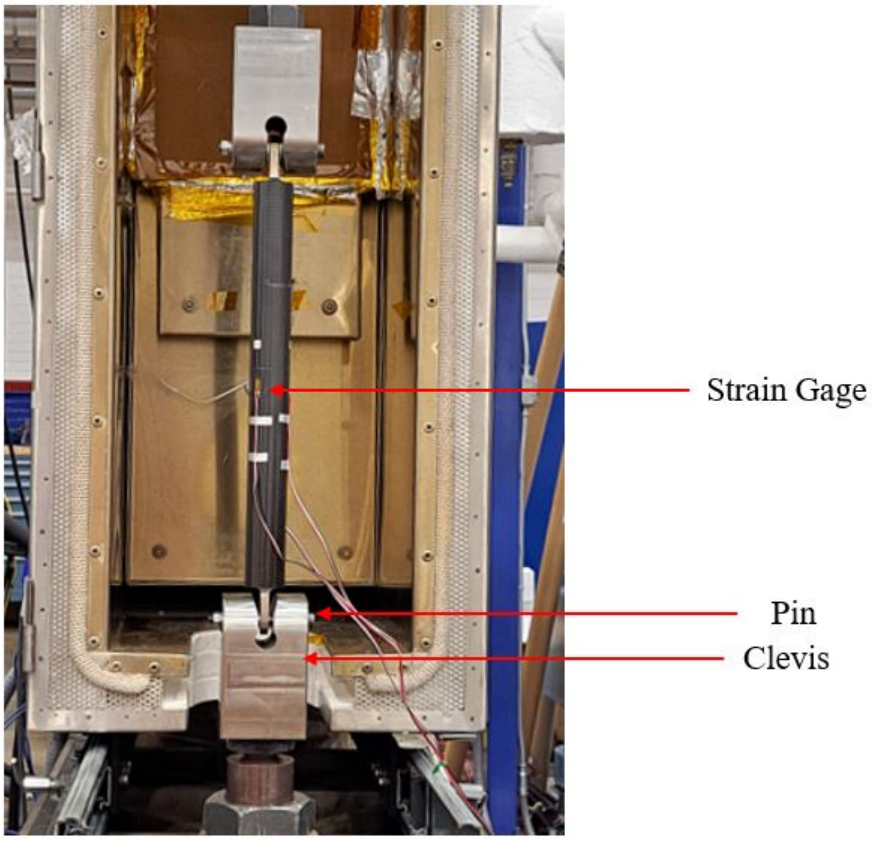

Figure 3. Modulus test setup

A summary of the tension-equivalent modulus data for the strut is shown in Table 1. The five specimens were labeled A-E, and data was collected for three trials. Each modulus displayed in the table for each trial was computed using the average of the three strain gages for the respective specimen. The last column in the table displays the average of the three trial modulus for each specimen. The average of the specimen moduli is given in red (bottom right). The stress versus

microstrain plot of the averaged sample data is shown in Fig. 4 for all five samples. This averaging process results in a tensile equivalent elastic modulus of 169 GPa. The manufacturer of the struts provided a tensile equivalent elastic modulus of 202 GPa.

Table 1. Tension-equivalent elastic modulus data (standard deviation of 6.20 GPa).

Specimen	Trial 1 (GPa)	Trial 2 (GPa)	Trial 3 (GPa)	Average (GPa)
A	177.72	178.62	178.60	178.31
B	168.65	168.34	168.50	168.50
C	171.96	172.17	172.21	172.11
D	163.42	164.02	163.72	163.72
E	164.14	164.13	163.51	163.92
Avg	-	-	-	169.32

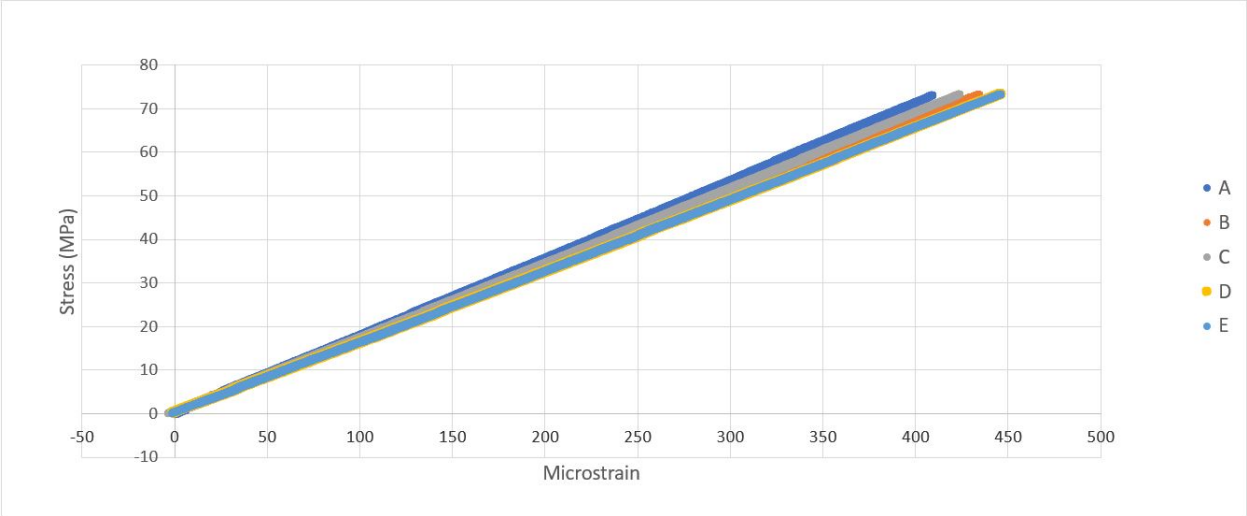

Figure 4. Average equivalent tension elastic modulus for strut.

The same procedure was followed to compute the compressive equivalent elastic modulus which resulted in 157 GPa. The results for the compression modulus data are summarized in Table 2. The manufacturer of the struts provided a compressive equivalent elastic modulus of 142 GPa. The stress versus microstrain data of the compressive averages are shown in Fig. 5 for all five samples. The value of 169 GPa was used in the analysis for struts that experienced tension, while 157 GPa was assigned to the struts that experienced compression in the test described in Chapter 3.

Table 2. Compression-equivalent elastic modulus data (standard deviation of 5.38 GPa).

Specimen	Trial 1 (GPa)	Trial 2 (GPa)	Trial 3 (GPa)	Average (GPa)
A	164.62	163.76	164.23	164.21
B	156.53	156.12	156.12	156.26
C	160.77	161.04	160.79	160.86
D	151.77	151.54	152.07	151.80
E	152.64	151.89	152.64	152.39
Avg	-	-	-	157.10

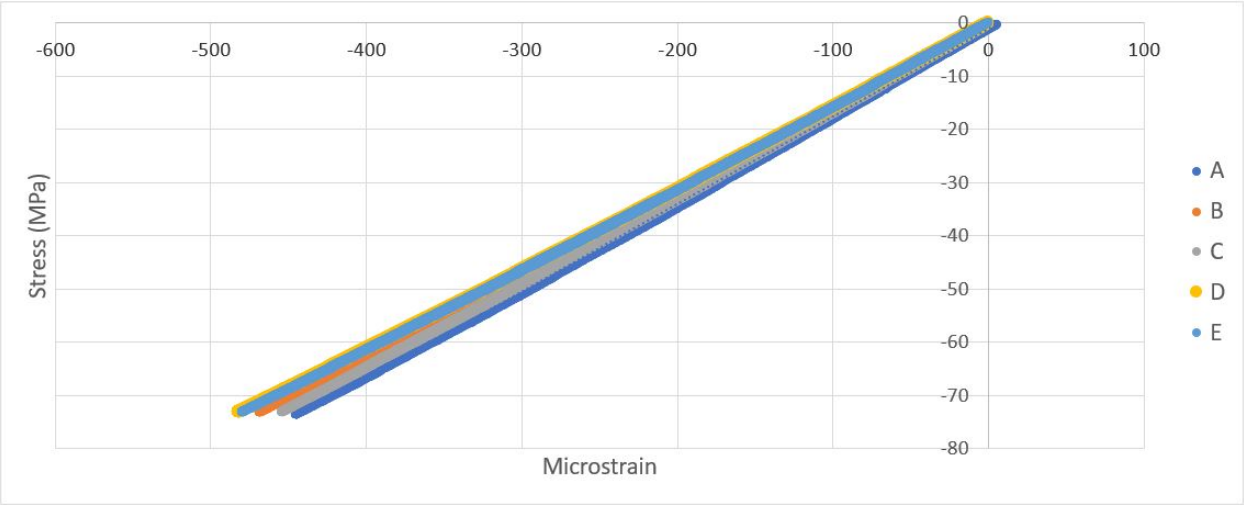

Figure 5. Average equivalent compression elastic modulus for strut.

Detailed plots showing each individual trial for all five specimens are shown in Ref. [21]. All trials gave linear data with an excellent line of fit and high R^2 values, and the slope of that line was recorded as the modulus for that given trial. The results from all three trials for each specimen were consistent, indicating that the first trial didn't influence the properties determined from the second and third trials. In Chapter 3, an overview of the TriTruss test setup and the finite element model will be discussed.

CHAPTER 3

TRITRUSS TEST SETUP AND FINITE ELEMENT MODEL

3.1 TRITRUSS TEST SETUP

The approach to the TriTruss test was to apply a static load to the TriTruss module to characterize the structural response. The TriTruss struts were thin-walled, hollow composite tubes made of Mitsubishi K63712 fibers in the axial direction and Mitsubishi 34-700 fibers in the hoop direction. Both materials use the same NB301 resin. The layup orientation was [0/90/90/0] and had a nominal thickness of 0.000889 m. The struts were joined to the joints by bonding the ends with an epoxy adhesive. An analysis was performed studying a variety of possible lifting configurations that would produce either an approximately 2000 N tension force or 1000 N compression force in the struts of the TriTruss module [22]. In order to avoid strut failure, no strut was to be subjected to more than 2000 N tension force or 1000 N compression force. The 2000 N tension force and 1000 N compression force were selected to be approximately half the value of measured strut failure loads at the time. The loading configuration was determined by analysis to apply a total load of 625.7 kg (6138 N) uniformly distributed to the bottom three joints of the TriTruss and was a sufficient method to achieve the desired loading configuration of each strut in the TriTruss. The loading configuration is shown in Fig. 6.

An illustration of the test setup is shown in Fig. 7. The setup included three sets of slings and shackles connecting the triangular spreader bar to the crane and then three more sets of shackles and vertical slings connecting the triangular spreader bar to a steel bracket installed on the TriTruss

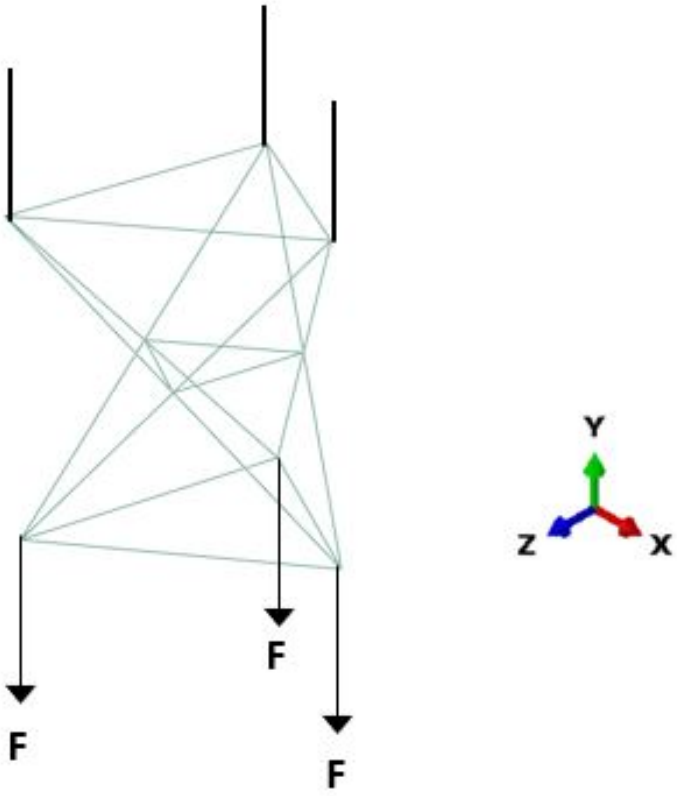

Figure 6. TriTruss loading configuration

top corner joints as shown in Fig. 7. The masses used to apply loading to the TriTruss module were suspended from the bottom of the TriTruss module. Additional shackles were located on the bottom of the TriTruss module with the same steel bracket attached to the bottom joints. An overhead crane was used to lift the assembly off the ground, thus initiating the loading of the TriTruss module. The masses were suspended on the TriTruss by fabricating custom made hangers. The mass hangers consisted of a steel rod with a custom made plate at the bottom, where all the masses were stacked, and an eye nut was installed at the top of the rod as depicted in Fig. 8. The shackles from the bottom TriTruss corners attached to the eye nut suspending the mass hangers from the module when the TriTruss was lifted. The mass hanger is shown in Fig. 8 with a 208.6 kg (2046 N) load that was applied to each of the three joints on the bottom triangle.

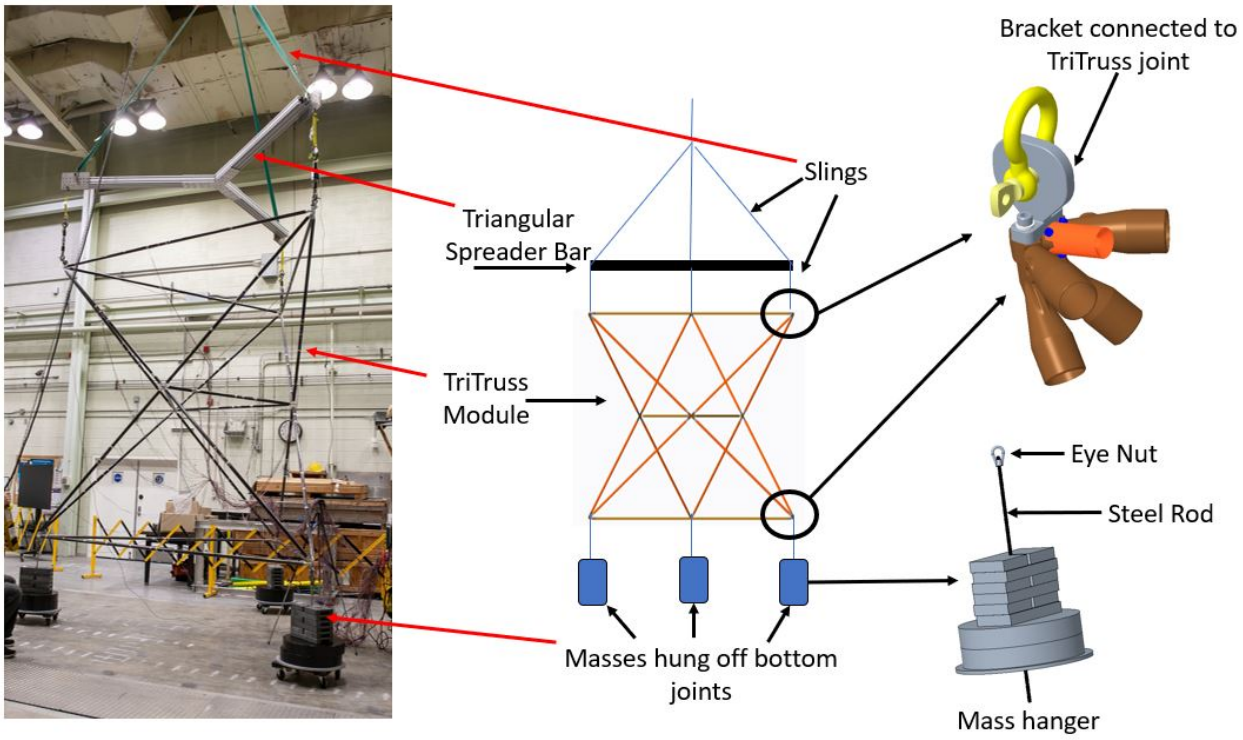

Figure 7. TriTruss test setup.

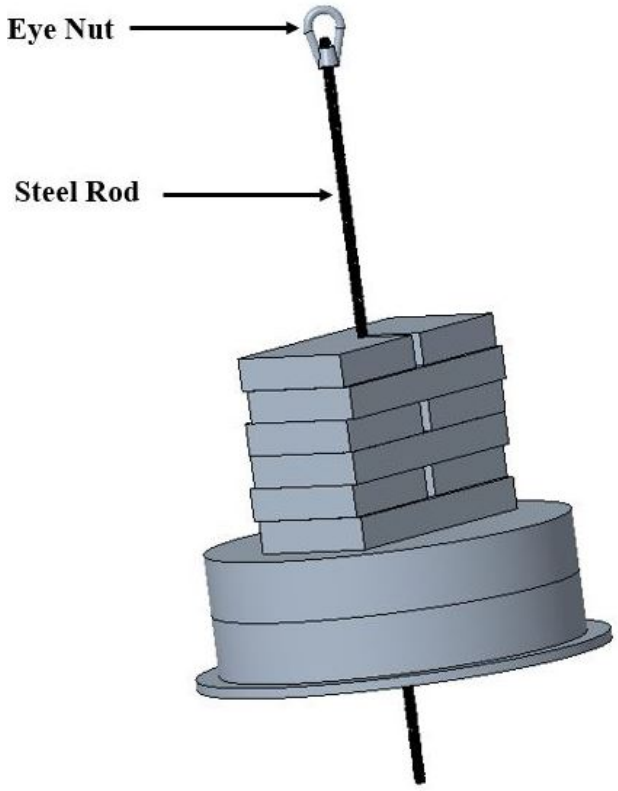

Figure 8. Mass hanger for loading configuration.

Strain gages were used with a data aquistion system to capture the response to the loading. A total of 42 biaxial strain gages were used on a TriTruss module. Two strain gages were placed at the center of each strut 180° apart as shown in Fig. 9, where the blue dots on the TriTruss represent the strain gage location (left) and the green circle represents the TriTruss strut cross-section (right) and the blue rectangles represent the strain gages on the cross-section. Induced strain in the struts were recorded, and the data were compared to strains extracted from the analysis. Each of the TriTruss struts was assigned an identifier to which the strain was mapped, as shown in Fig. 10. The struts that make up the top triangle are noted as Top1, Top2, and Top3. A similar designation was used for the middle triangle and the bottom triangle in the TriTruss. The diagonal struts in the top half of the TriTruss are labeled "DT", and the diagonal struts in the bottom half are labeled "DB". A number system was assigned to each of these diagonal struts.

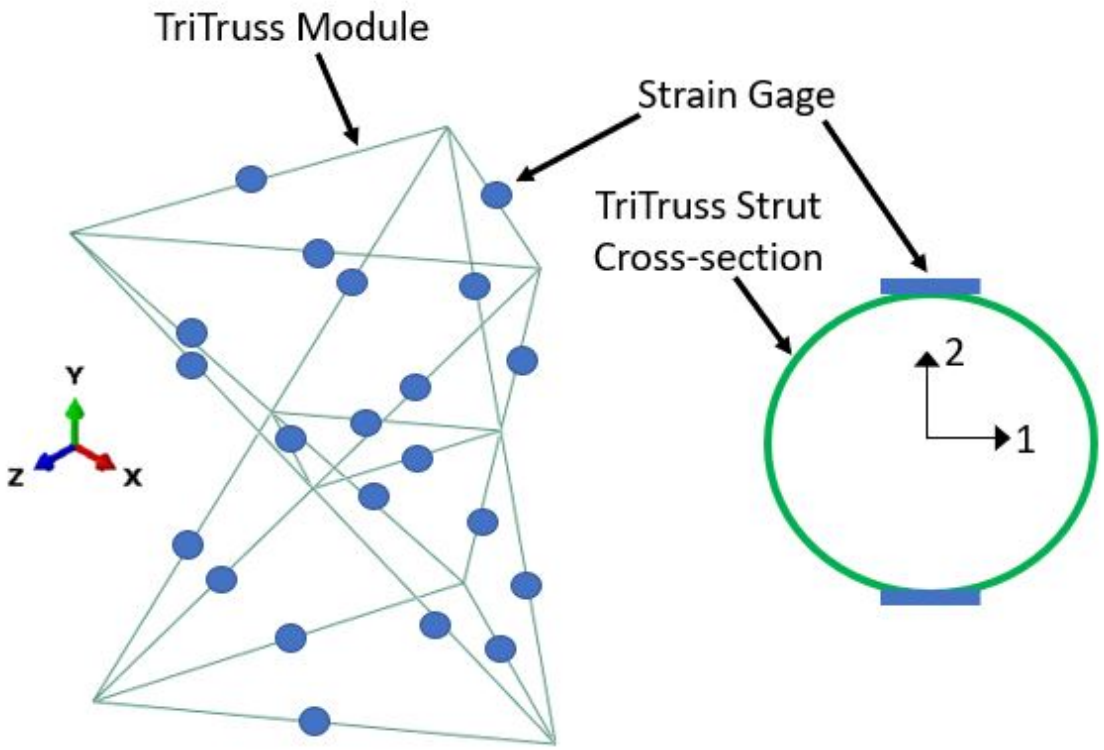

Figure 9. Strain gage placement on TriTruss module.

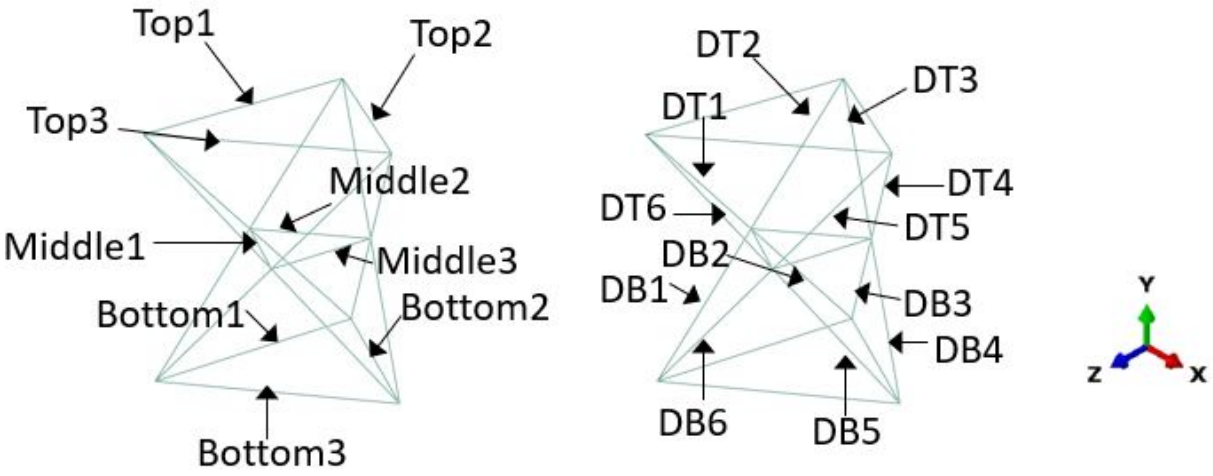

Figure 10. Nomenclature used for strut numbering.

3.2 FINITE ELEMENT MODEL

A linear, static finite element analysis was performed using commercially available Abaqus software[1]. A finite element model of a single TriTruss module was developed and analyzed to predict the average axial strain in all 21 struts. Beam elements, B31, were used to model the joints and the struts which were assumed to be perfectly connected at the joints; no overlap of the strut beam elements and joint beam elements was modeled. After a mesh convergence study was conducted, each strut was composed of 4 beam elements and each joint was made up of a total of 4 beam elements that all connected at the corner node of the TriTruss via a shared node. There were a total of 126 elements and 114 nodes that made up the TriTruss FEM. The struts were assigned a pipe profile with an outer radius of 0.015193 m and a thickness of 0.001000076 m by taking measurements of the strut. The length of the top struts was 2.8 m, middle struts was 1.42 m, bottom struts was 2.9 m, top diagonal struts was 1.96 m, and bottom diagonal struts was 2.03 m. The joints were also assigned a pipe profile with an outer radius of 0.0152 m and a thickness of 0.00089 m. The three nodes at the corners of the top triangle were all fixed in translation and rotation about the global Y-axis. A load of 208.6 kg (2046 N) was applied to each corner on the bottom triangle in the global negative Y-direction. An illustration of the FEM is shown in Fig. 11 where the red dots represent where the boundary conditions were applied. The mesh with the boundary conditions, node labels, and element labels is shown in Figs. 12-14. Since the diagonal struts experienced tension and the top, middle, and bottom struts experienced compression based on the test results, the average tensile and compressive Young's modulus computed from previously collected experimental data were assigned to the respective struts isotropically since this was an

[1]The use of trademarks or names of manufacturers in this report is for accurate reporting and does not constitute an official endorsement, either expressed or implied, of such products or manufacturers by the National Aeronautics and Space Administration.

equivalent elastic modulus. The diagonal struts of the TriTruss were assigned a Young's modulus of 169 GPa, and the top, middle, and bottom struts were assigned a Young's modulus of 157 GPa. The joints were assigned generic aluminum material properties, a Young's modulus value of 68.9 GPa, for this analysis. The material property sections on the TriTruss are shown in Fig. 15. In Chapter 4, the results will be presented and compared to analysis, as well as adjustments that were made to the finite element model including a strut imperfection analysis. Then, a discussion of the experiment and analysis will be presented.

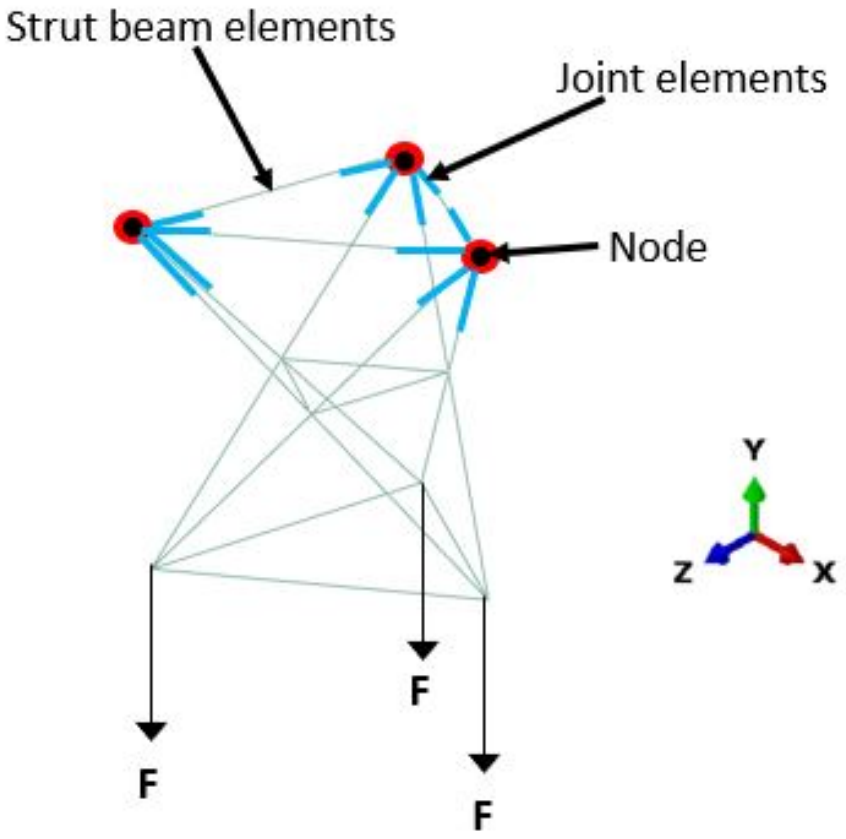

Figure 11. Finite element model of TriTruss.

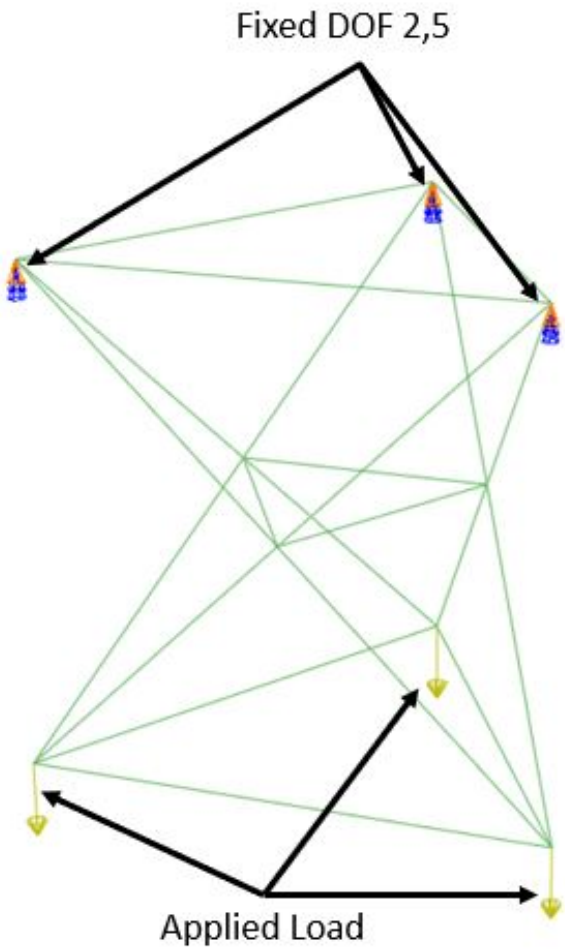

Figure 12. Boundary conditions and applied load.

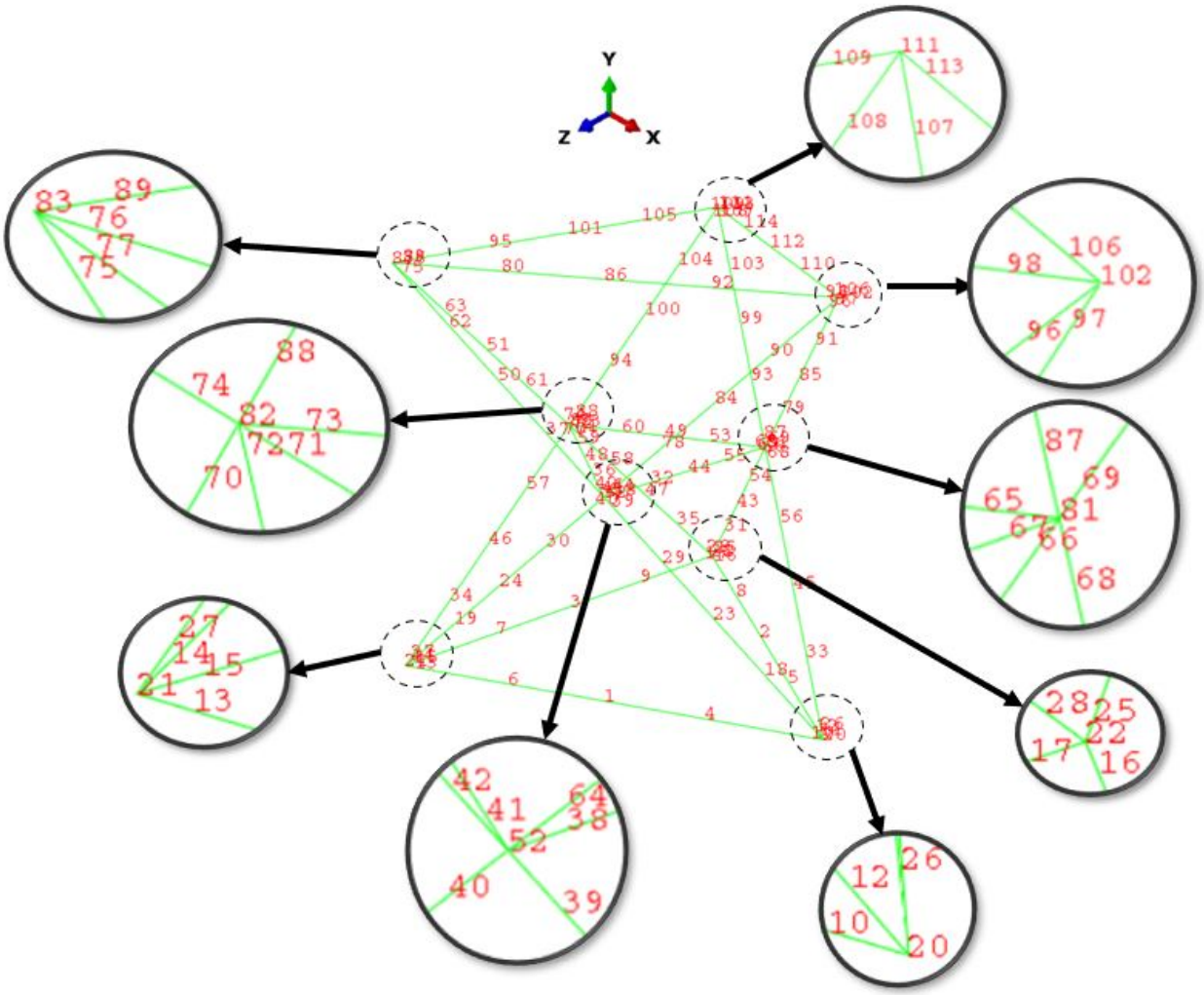

Figure 13. Node labels.

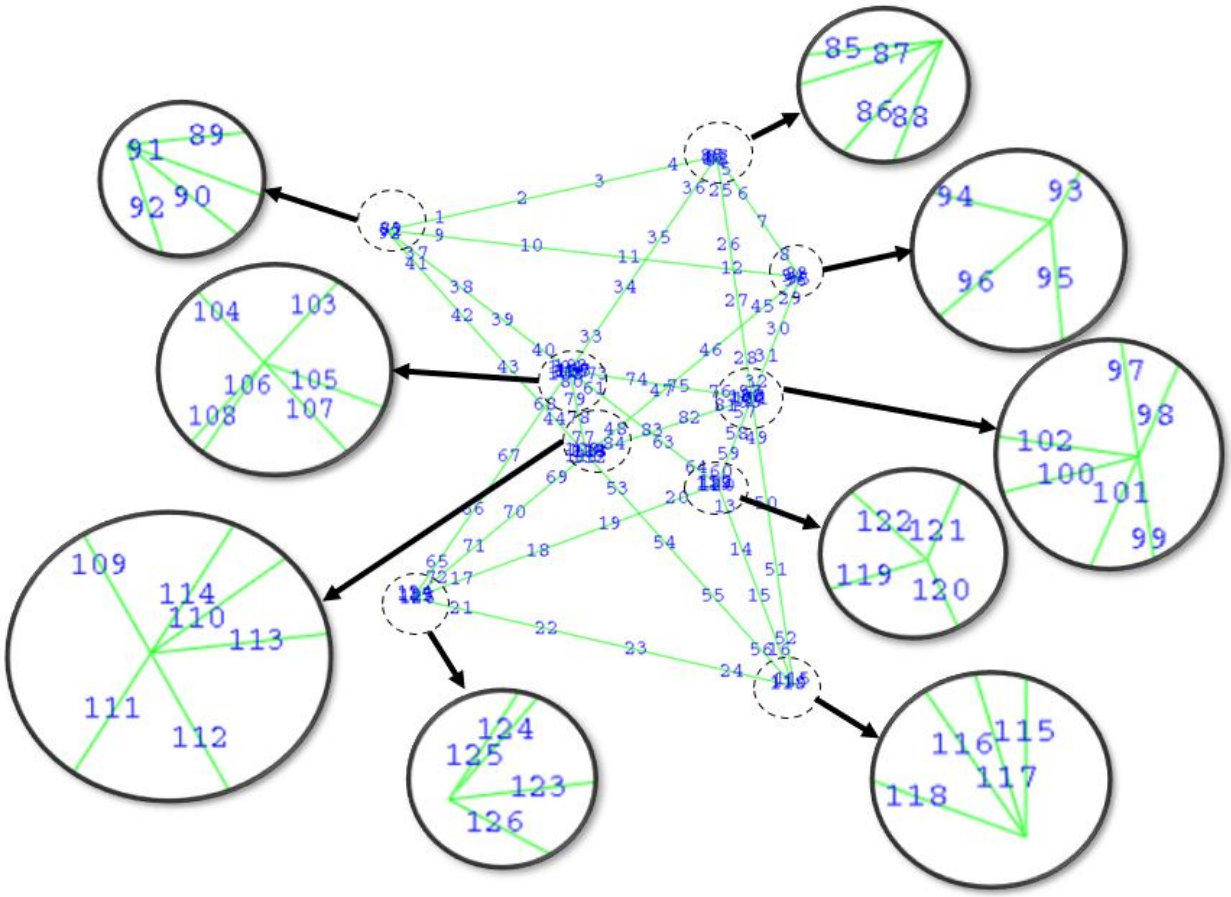

Figure 14. Element labels.

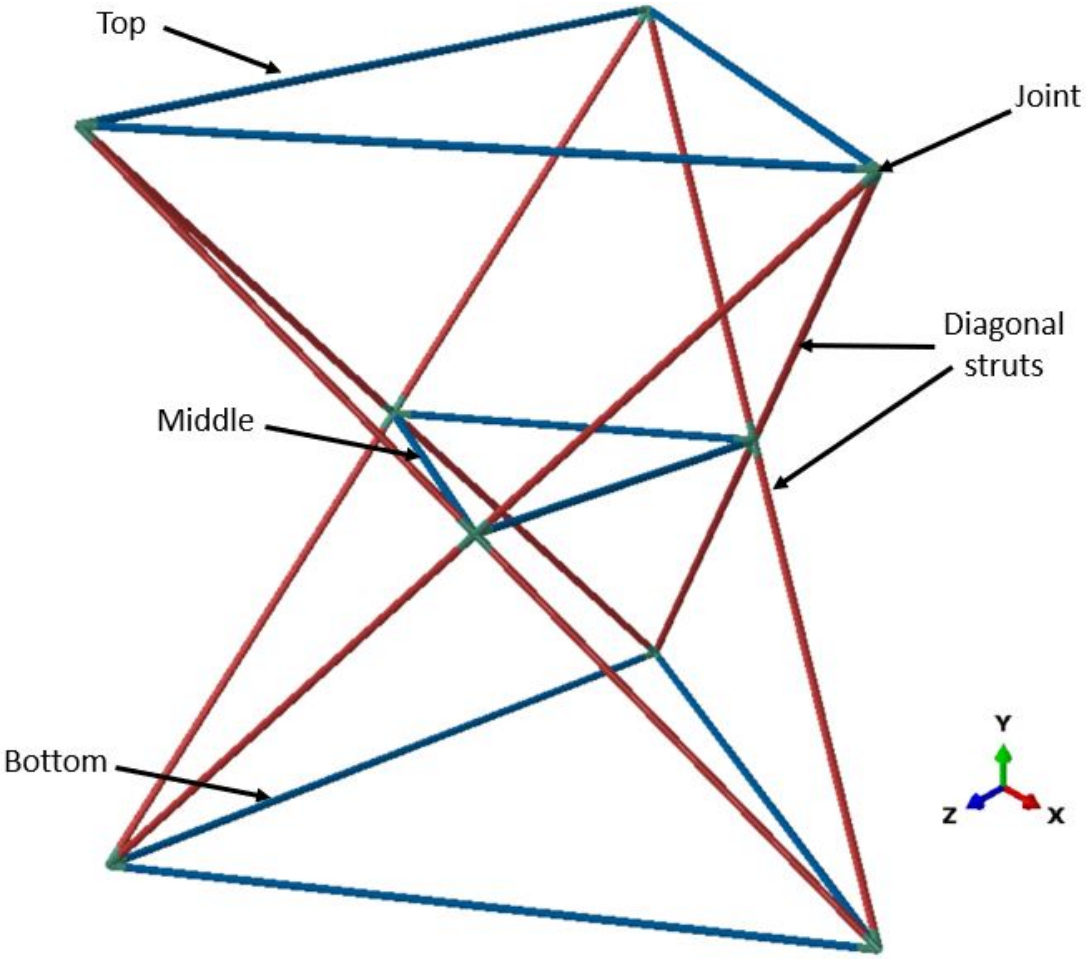

Figure 15. Material properties for TriTruss.

CHAPTER 4

RESULTS AND DISCUSSION

4.1 RESULTS

The experiment was conducted, and microstrain values for each strut were collected. The TriTruss module was lifted and suspended for about a minute to ensure the strains remained relatively constant before lowering the TriTruss module back to the ground. The time history for the microstrain is shown in Fig. 16. The strain gages were denoted with a "_1" and "_2" to indicate the first strain gage and the second strain gage on the strut, respectively. Since each strut had two strain gages, the two values were averaged for each strut and recorded using the values extracted at the 100 s mark. The data was recorded at this point since it was about the midpoint of the time history and the strains were relatively constant at this point. The time histories for the strain in the Top, DT, DB, and Bottom struts are shown in Figs. 17-20, respectively. There was suspected to be a significant amount of bending in the top and bottom struts (Fig. 17 and Fig. 20) since the strain gage time histories for a particular strut have a gap in their data. For example, looking at the Bottom1 strut in Fig. 20, the red line and the orange line have a sizable gap between them, indicating bending may be occurring in the strut. For the diagonal struts, (Fig. 18 and Fig. 19), the strain gage time histories for a particular strut are lined up with each other more, indicating mostly axial loading. For example, looking at the DT2 strut in Fig. 18, the red line and the gray line are lined up with each other more, indicating axial load in the strut. For the analysis, the average strains were reported by averaging around integration points 1, 3, 5, and 7 of the four

B31 beam elements in each strut (Fig. 21). Microstrain values from the experiment and analysis for the middle triangle were zero in the analysis, and the data collected from the experiment was mainly noise; therefore, it will not be a relevant comparison, and microstrain results from the test and analysis are presented for just the top and bottom struts and all the diagonal struts. The goal for the characterization study was to achieve a correlation within 10% between the test data and the analysis. The test and analysis results along with the percent difference are shown in Table 3. The deflection (m), stress (Pa), and strain contour plots are shown in Fig. 22. Overall, the test and analysis have good correlation with 13 of the struts being lower than 10% and with ten of those 13 struts lower than 5%. However, there are five struts out of 18, highlighted in Table 3, that go over the targeted 10% difference. There were a few possibilities that were taken into consideration to account for the higher percent difference in the five struts.

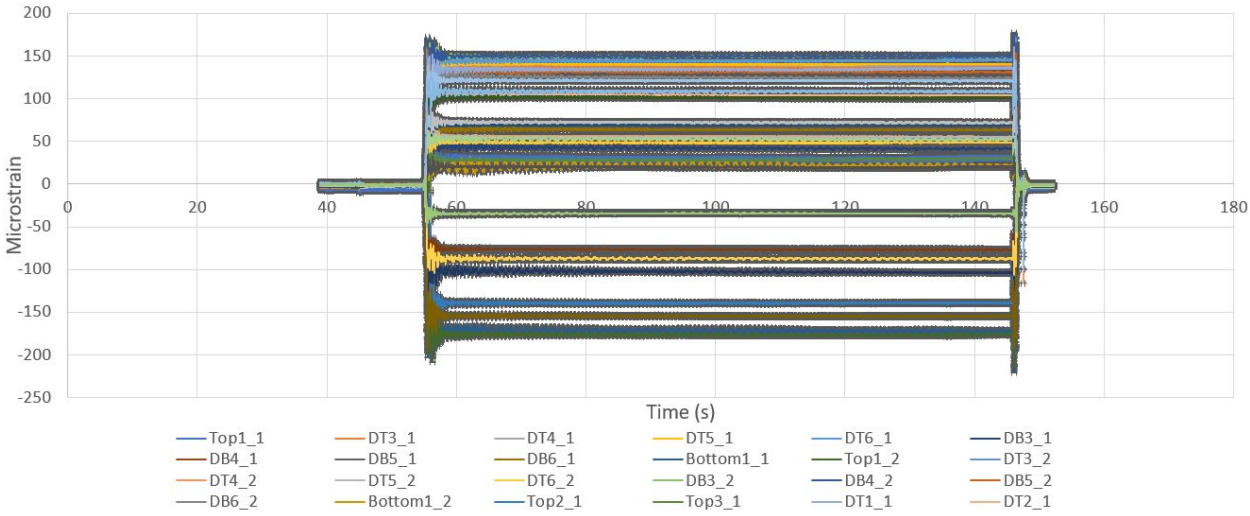

Figure 16. Time history of strain gages.

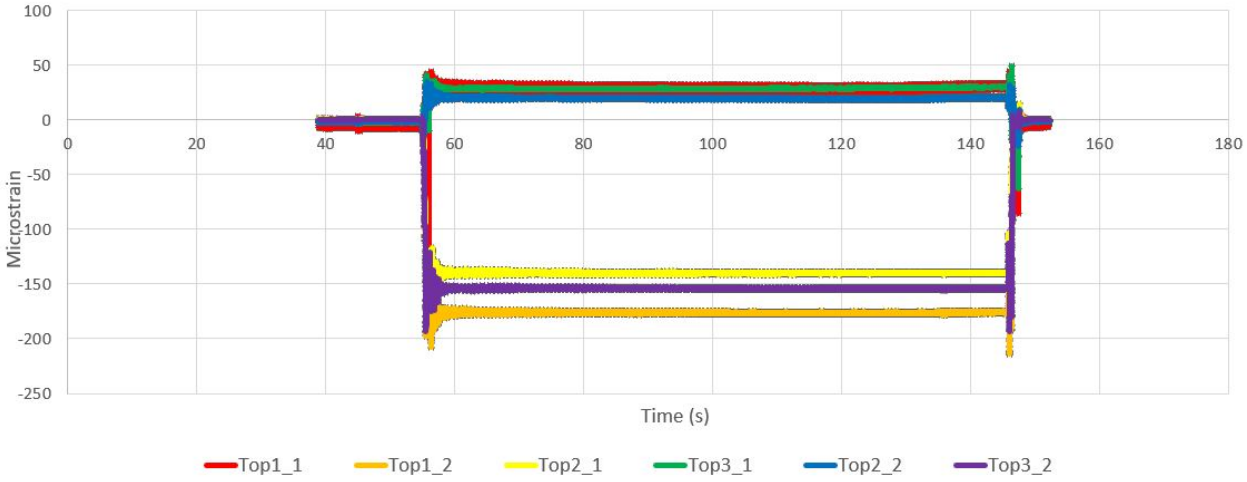

Figure 17. Time history of Top strain gages.

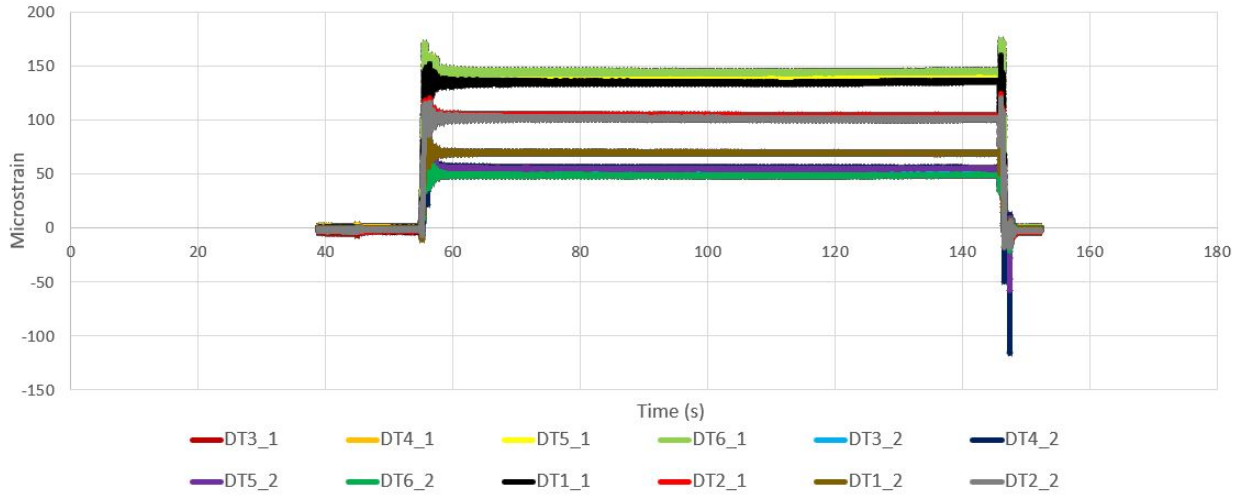

Figure 18. Time history of DT strain gages.

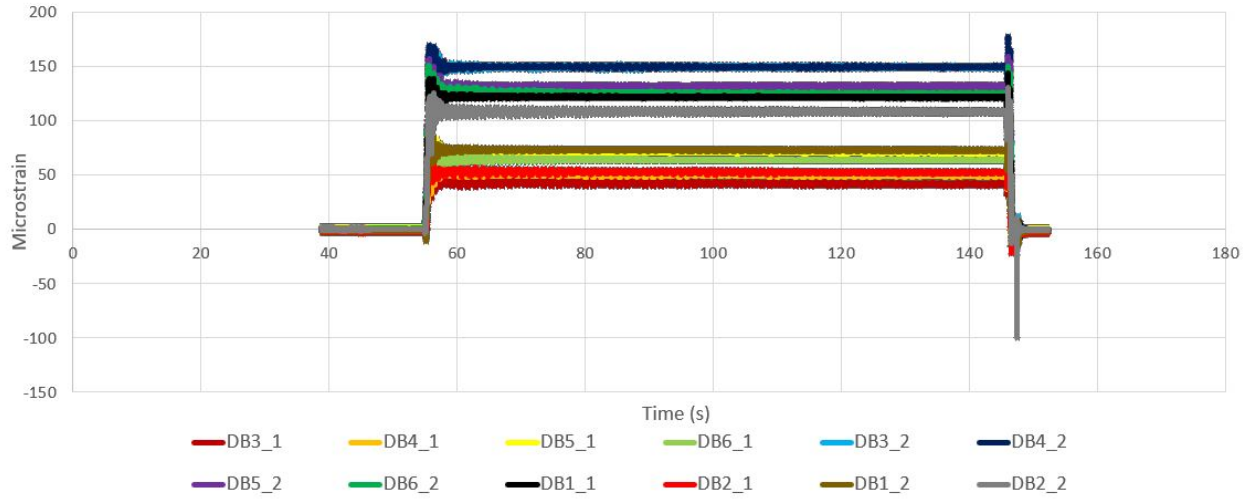

Figure 19. Time history of DB strain gages.

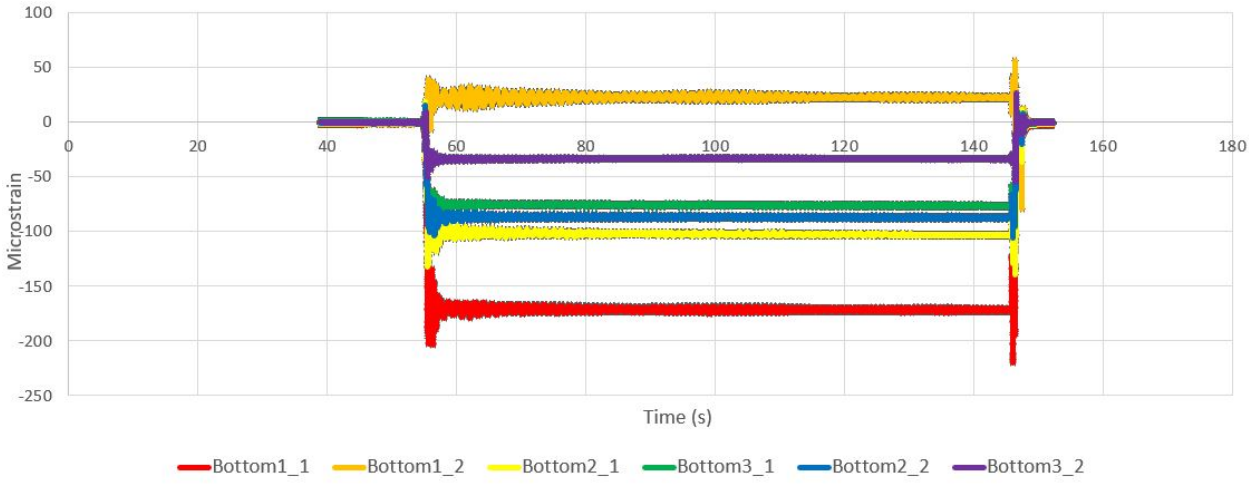

Figure 20. Time history of Bottom strain gages.

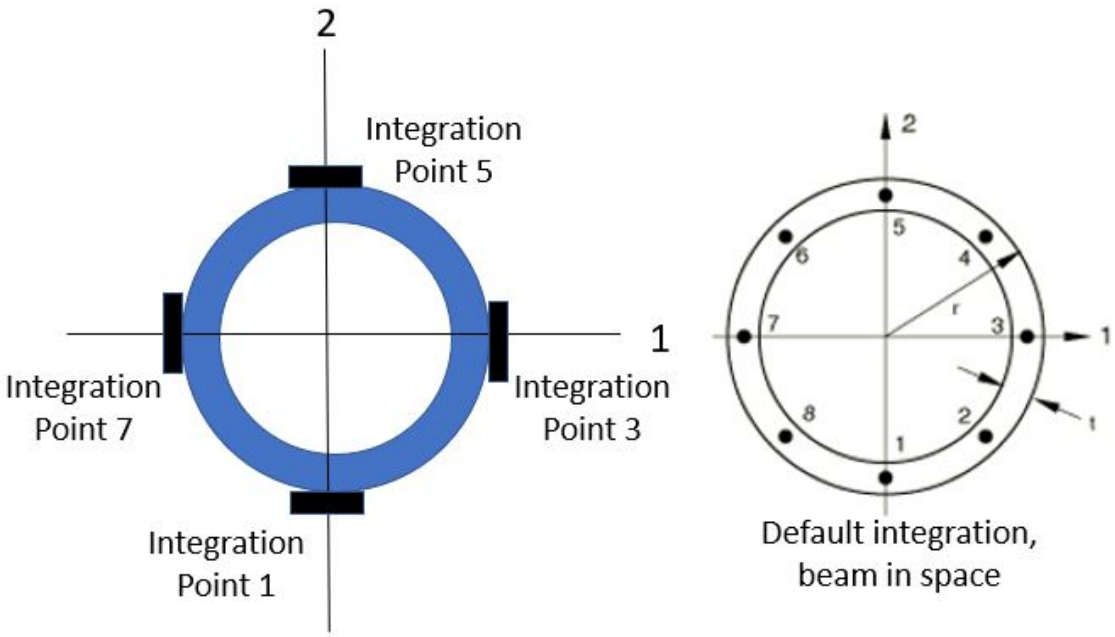

Figure 21. Beam integration points on pipe profile [23].

Table 3. Test and analysis results for microstrain in struts using average modulus.

	Experimental Microstrain	Analytical Microstrain	% Difference
Top1	-72.5	-71.7	1.10
Top2	-59.5	-72.4	21.68
Top3	-63.0	-72.4	14.92
Bottom1	-75.0	-72.6	3.20
Bottom2	-94.5	-73.2	22.54
Bottom3	-55.5	-73.2	31.89
DT1	101.5	94.1	7.29
DT2	103.0	94.1	8.64
DT3	96.0	94.9	1.15
DT4	97.5	94.9	2.67
DT5	97.5	94.9	2.67
DT6	97.0	94.9	2.16
DB1	97.0	94.1	2.99
DB2	81.0	94.1	16.17
DB3	96	94.9	1.15
DB4	99.5	94.9	4.62
DB5	101.0	94.9	6.04
DB6	94.0	94.9	0.96

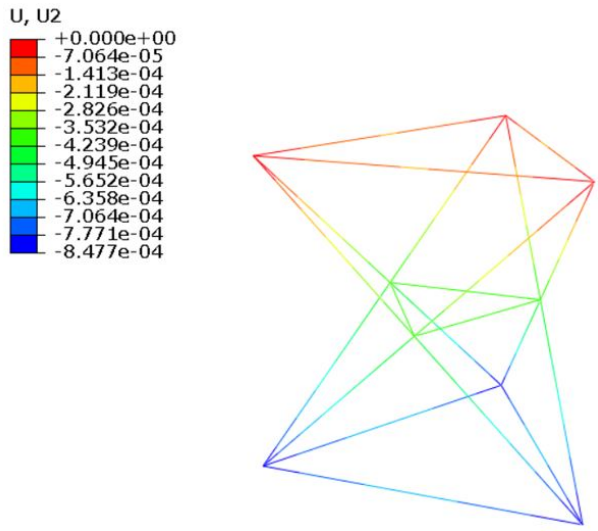

(a) Deflection contour plot

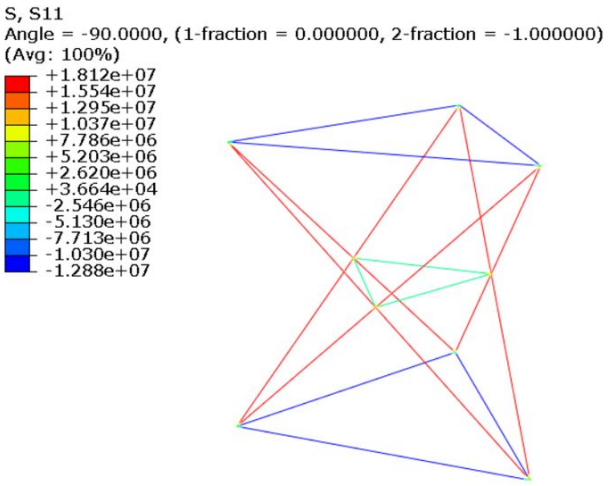

(b) Axial stress contour plot

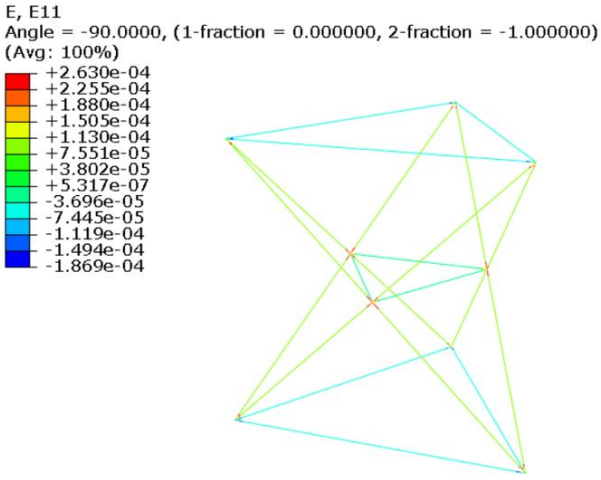

(c) Axial strain contour plot

Figure 22. Baseline analysis contour plots.

4.2 ADJUSTMENTS IN FINITE ELEMENT MODELING

The first consideration in modifying the analysis to better align with the test results was to adjust the tensile and compressive elastic moduli. Since the analysis results, shown in Table 3, were for a model that used the average tensile modulus in the diagonal struts and the average

compressive modulus in the top and bottom struts, a study was conducted to investigate how using the smallest and largest tensile or compressive modulus that was found in the experimental data affected the results. The first study was only changing the tensile modulus in the diagonal struts while keeping the compressive modulus the same in the top and bottom struts, shown in Table 4. The only diagonal strut above 10% error, DB2, in the analysis results in Table 3 was at 16.17% error. When using the higher tensile modulus from the test data, the percent difference decreases to 10.25%. Since the other eleven diagonal struts are under 10% and varying the tensile modulus decreased the difference in DB2 to a more reasonable error, this result for DB2 is considered acceptable and is successfully characterized with the other diagonal struts. The second study was only changing the compressive modulus in the top and bottom struts while keeping the tensile modulus at its baselined average in the diagonal struts. These results are summarized in Table 5. In Table 3, Top2, Top3, Bottom2, and Bottom3 are all above 10% error. Overall, it appeared that using the lower tested compressive modulus made the error worse and using the higher tested compressive modulus helped reduce the difference. Top2, Top3, and Bottom3 all decreased in error with Top3 going down to the accepted 10% error. The deflection (m), stress (Pa), and strain contour plots using the higher tested compressive modulus are shown in Fig. 23. The results for these studies leave three struts, Top2, Bottom2, and Bottom3, still higher than the accepted error threshold.

Another consideration to account for the higher error in the remaining three struts was analyzing an angled force scenario if the applied forces were not exactly vertical. An analysis was done that applied a downward angled weight of 10° towards the structure to one of the three nodes on the bottom of the TriTruss in the global X-Y plane. The analysis resulted in much higher and unrealistic errors in several struts compared to the actual experiment; therefore, the results will not

be presented for this analysis.

Table 4. Varying tensile modulus in diagonal struts.

	Experimental Microstrain	Low Tensile E Microstrain (E=163.7 GPa)	% Difference	High Tensile E Microstrain (E=178 GPa)	% Difference
Top1	-72.5	-71.7	1.10	-71.7	1.10
Top2	-59.5	-72.4	21.68	-72.4	21.68
Top3	-63.0	-72.4	14.92	-72.4	14.92
Bottom1	-75.0	-72.6	3.20	-72.6	3.20
Bottom2	-94.5	-73.2	22.54	-73.2	22.54
Bottom3	-55.5	-73.2	31.89	-73.2	31.89
DT1	101.5	97.1	4.33	89.3	12.02
DT2	103.0	97.1	5.73	89.3	13.30
DT3	96.0	98	2.08	90.1	6.15
DT4	97.5	98	0.51	90.1	7.59
DT5	97.5	98	0.51	90.1	7.59
DT6	97.0	98	1.03	90.1	7.11
DB1	97.0	97.1	0.10	89.3	7.94
DB2	81.0	97.1	19.88	89.3	10.25
DB3	96	98	2.08	90.1	6.15
DB4	99.5	98	1.51	90.1	9.45
DB5	101.0	98	2.97	90.1	10.79
DB6	94.0	98	4.26	90.1	4.15

Table 5. Varying compressive modulus in top and bottom struts.

	Experimental Microstrain	Low Compressive E Microstrain (E=151.8 GPa)	% Difference	High Compressive E Microstrain (E=164 GPa)	% Difference
Top1	-72.5	-74.2	2.34	-68.7	5.24
Top2	-59.5	-74.9	25.88	-69.3	16.47
Top3	-63.0	-74.9	18.89	-69.3	10.00
Bottom1	-75.0	-75.1	0.13	-69.5	7.33
Bottom2	-94.5	-75.8	19.79	-70.1	25.82
Bottom3	-55.5	-75.8	36.58	-70.1	26.31
DT1	101.5	94.1	7.29	94.1	7.29
DT2	103.0	94.1	8.64	94.1	8.64
DT3	96.0	94.9	1.15	94.9	1.15
DT4	97.5	94.9	2.67	94.9	2.67
DT5	97.5	94.9	2.67	94.9	2.67
DT6	97.0	94.9	2.16	94.9	2.16
DB1	97.0	94.1	2.99	94.1	2.99
DB2	81.0	94.1	16.17	94.1	16.17
DB3	96	94.9	1.15	94.9	1.15
DB4	99.5	94.9	4.62	94.9	4.62
DB5	101.0	94.9	6.04	94.9	6.04
DB6	94.0	94.9	0.96	94.9	0.96

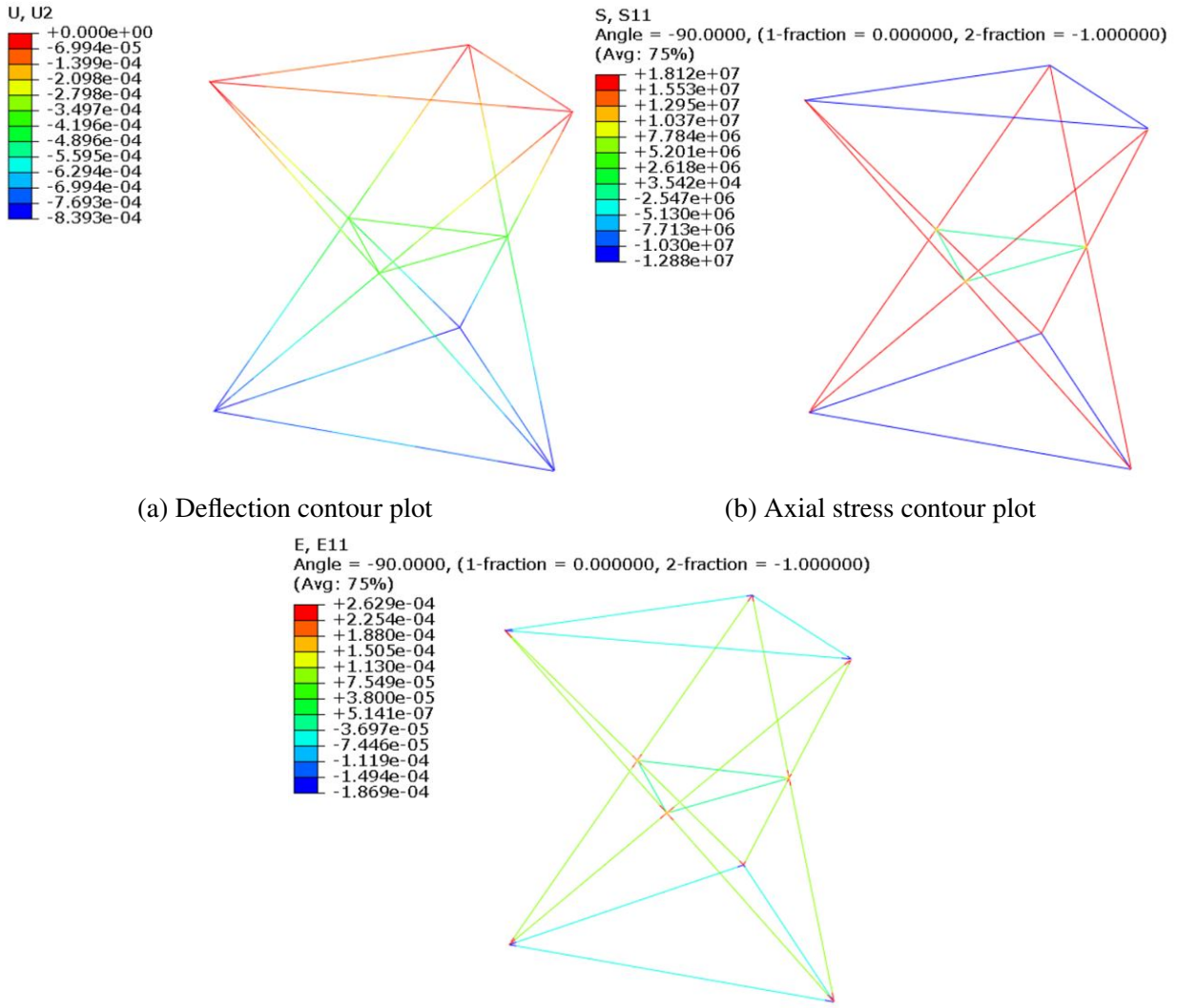

(a) Deflection contour plot

(b) Axial stress contour plot

(c) Axial strain contour plot

Figure 23. Contour plots using higher tested compressive modulus.

The last consideration for the global model that was analyzed was a potential applied moment at the joint where the load was applied. In the FEM, the load is applied at an exact point which is meant to be the end of the joint whereas the experiment had the load applied at an offset of about 0.0127-0.0254 m from the actual end point of the joint, towards the inside of the TriTruss. An illustration of this is shown in Fig. 24. The green rectangles represent the TriTruss, and the

blue rectangles represent the joint. The orange circle is the node in the FEM where the force was applied. The bracket is represented by the red rectangle in Fig. 24, and this is the location where the force was applied in the experiment. This creates an offset distance from the FEM which is about 0.0127-0.0254 m. Since the force was 2046 N, this creates a moment between 26 N-m and 52 N-m. Both of these moments were created in the FEM and analyzed. The results are shown in Table 6. The application of these moments did not improve the results much, and there are still three struts–Top2, Bottom2, and Bottom3–greater than the 10% error threshold.

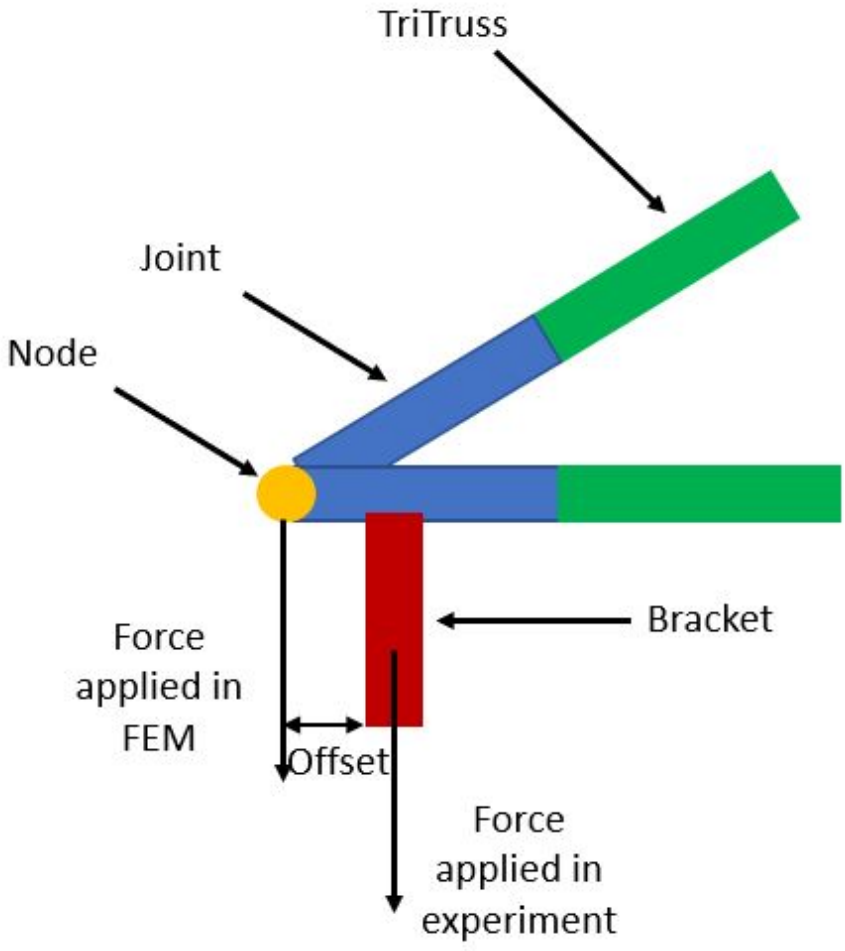

Figure 24. TriTruss configuration for applied moment.

Table 6. Applied moment results.

	Experimental Microstrain	26 N-m Moment Microstrain	% Difference	52 N-m Moment Microstrain	% Difference
Top1	-72.5	-68.3	5.74	-68.0	6.26
Top2	-59.5	-69.0	15.90	-68.6	15.24
Top3	-63.0	-70.1	11.27	-70.9	12.49
Bottom1	-75.0	-68.8	8.23	-68.1	9.20
Bottom2	-94.5	-69.4	26.53	-68.7	27.30
Bottom3	-55.5	-70.9	27.73	-71.6	29.06
DT1	101.5	93.6	7.83	93.0	8.35
DT2	103.0	93.6	9.16	93.1	9.65
DT3	96.0	94.4	1.68	93.9	2.21
DT4	97.5	94.4	3.20	93.9	3.74
DT5	97.5	96.0	1.59	97.0	0.52
DT6	97.0	95.9	1.09	97.0	0.02
DB1	97.0	93.2	3.96	92.2	4.91
DB2	81.0	93.5	15.46	93.0	14.75
DB3	96	94.4	1.72	93.8	2.31
DB4	99.5	94.0	5.55	93.1	6.47
DB5	101.0	96.0	4.99	97.0	3.94
DB6	94.0	96.0	2.10	97.0	3.21

4.3 STRUT IMPERFECTION ANALYSIS

The last item that was investigated was a potential influence of imperfections in the struts. A slight bow that could exist in the strut due to manufacturing processes would affect the strains produced in the struts, particularly the top and bottom struts since bending is suspected to be occurring according to Fig. 17 and Fig. 20. The purpose of this study was to determine imperfection magnitudes that may be influencing the remaining strain discrepancies in the struts. For this analysis, hand calculations were performed on a single TriTruss strut with the same geometry and material properties. Since two of the bottom struts have the highest remaining error, the length, l, for these struts (2.9 m) was used in the analysis. Ref. [24] was used to determine an expression for lateral

displacement of a compressively loaded, simply-supported strut with the assumption of a parabolic initial imperfection. The deformed shape $w(x)$ of a strut with an initial imperfection shape $w_0(x)$ acted on by a compressive axial load P applied at a distance e from the neutral axis is shown in Fig. 25 [24] where $\delta(x)$ is the total lateral displacement.

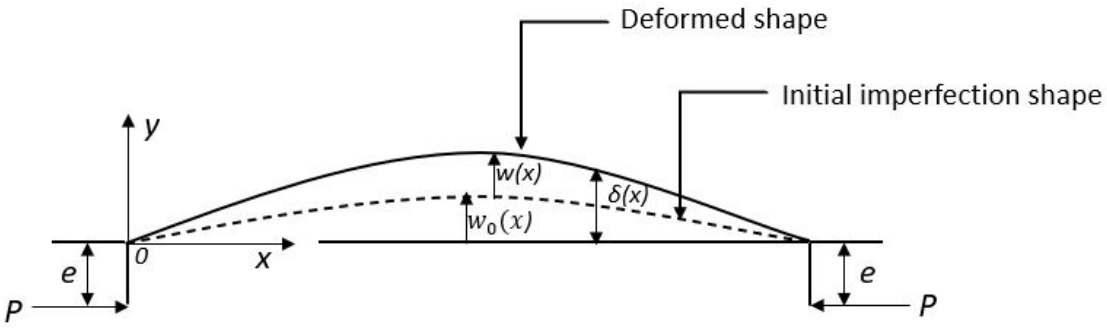

Figure 25. Axial compression of an initially imperfect strut with eccentric end loads.

The linear differential equation to determine $w(x)$ is:

$$EI\frac{d^2w}{dx^2} + Pw = -P(w_0 + e) \tag{1}$$

where simply-supported conditions result in

$$w(0) = w(l) = 0 \tag{2}$$

The solution to the homogeneous portion of equation (1) after applying the simply supported boundary conditions gives:

$$w_h = B_1 cos(\pi\sqrt{q}\frac{x}{l}) + B_2 sin(\pi\sqrt{q}\frac{x}{l}) \tag{3}$$

where B_1 and B_2 are determined from the boundary conditions and q is the compressive axial load normalized by the Euler buckling load and is defined by:

$$q = \frac{P}{P_e} = \frac{Pl^2}{\pi^2 EI} \tag{4}$$

where E is Young's modulus, and I is the area moment of inertia. The initial imperfection shape $w_0(x)$ is assumed to be parabolic in Ref. [24], and that was used in this study as well, with maximum magnitude μ given by:

$$w_0(x) = 4\mu\left[\frac{x}{l} - (\frac{x}{l})^2\right] \tag{5}$$

Substituting equation (5) into equation (1), determining the particular solution, and applying the simply-supported boundary conditions results in the following expression for lateral displacement of a compressively loaded strut with an initial parabolic imperfection [24]:

$$w(x) = \frac{8\mu}{\pi^2 q}\left(\frac{\pi^2 qx^2}{2l^2} - \frac{\pi^2 qx}{2l} - 1\right) + \left(\frac{8\mu}{\pi^2 q} + e\right)\left[tan\left(\frac{\pi\sqrt{q}}{2}\right)sin\left(\frac{\pi\sqrt{q}x}{l}\right) + cos\left(\frac{\pi\sqrt{q}x}{l}\right)\right] - e \tag{6}$$

The total lateral displacement, $\delta(x)$, is the sum of the initial imperfection shape and the deformed shape:

$$\delta(x) = w_0(x) + w(x) \tag{7}$$

Using Bernoulli-Euler Beam Theory:

$$EI\frac{d^2\delta}{dx^2} = M(x) \tag{8}$$

the moment, $M(x)$, can be solved for the initially imperfect strut. Since the maximum δ would occur at the center of the strut, the $M(x)$ equation was solved at $x = 1.45$ m to obtain the maximum moment. A positive point moment is also acting on the strut by taking the cross product of P and e. The total moment would then be:

$$M_{tot} = M(x) + Pe \tag{9}$$

The stress, σ, can then be computed at the top and bottom of the strut using the equations:

$$\sigma_t = \frac{-M_{tot}y}{I} - \frac{P}{A}, \quad \sigma_b = \frac{M_{tot}y}{I} - \frac{P}{A} \tag{10}$$

where σ_t is the stress at the top of the strut, σ_b is the stress at the bottom of the strut, y is the perpendicular distance from the neutral axis to a point on the section, and A is the cross-sectional area of the strut. Then, the top and bottom strains were computed using the equations:

$$\varepsilon_t = \frac{\sigma_t}{E}, \quad \varepsilon_b = \frac{\sigma_b}{E} \tag{11}$$

where ε_t and ε_b are the top and bottom strains, respectively. To investigate the effect of initial

imperfections and load eccentricities, various values for μ and e were analyzed to see how they affect the top and bottom strains on the strut. Each of the bottom three struts in the experiment were studied to evaluate the effects of initial imperfections and load eccentricities.

The load in the Bottom1 strut can be calculated by taking the experimental microstrain value and multiplying it by the product of the average elastic modulus from the experimental data and the cross-sectional area of the strut. This calcluation results in a load of -1157 N in the Bottom1 strut. The two microstrain values recorded were -171 and 21. This -1157 N load was used as P in all of the equations above. Values for μ and e are shown in meters and ε_t and ε_b are the microstrain values. The results are shown in Table 7. For the Bottom1 strut, it was found that an initial imperfection value of 0.00161 m and load eccentricity of 0.00115 m were the values that best replicate the experimental strain in the Bottom1 strut.

Table 7. Imperfection results for Bottom1 strut.

μ (m)	e (m)	ε_t	ε_b
0	0	-79.8	-79.8
0	0.001	-55.9	-103.7
0.001	0	-34.5	-125.0
0.001	0.001	-10.6	-149.0
0.002	0.002	58.6	-218.1
0.00161	0.00115	20.6	-180.1
Experimental Microstrain		21	-171

The Bottom2 strut experienced a load of -1458 N in the experiment, and the two microstrain values recorded were -103 and -86. The results are shown in Table 8. For the Bottom2 strut, it was

found that an initial imperfection value of 0.00008 m and load eccentricity of 0.00008 m were the values that best replicate the experimental strain in the Bottom2 strut.

Table 8. Imperfection results for Bottom2 strut.

μ (m)	e (m)	ε_t	ε_b
0	0	-100.5	-100.5
0	0.001	-32.2	-168.8
0.001	0	-16.2	-184.8
0.00008	0.00008	-88.3	-112.7
Experimental Microstrain		-86	-103

The Bottom3 strut experienced a load of -856 N in the experiment, and the two microstrain values recorded were -77 and -34. The results are shown in Table 9. For the Bottom3 strut, it was found that an initial imperfection value of 0.00073 m and load eccentricity of 0.00053 m were the values that best replicate the experimental strain in the Bottom3 strut.

The strains for ε_t and ε_b could not be matched exactly since trying to replicate one value would significantly increase the difference for the other, so the goal was to get as close to the experimental values as reasonable. These initial imperfection and load eccentricity values indicate that, for a 2.9-m strut, there could be a very small bow in the structure when manufactured and should be considered in future analyses.

Table 9. Imperfection results for Bottom3 strut.

μ (m)	e (m)	ε_t	ε_b
0	0	-59.0	-59.0
0	0.001	-28.8	-89.2
0.001	0	-50.0	-68.1
0.00073	0.00053	-36.4	-81.6
Experimental Microstrain		-34	-77

4.4 DISCUSSION

Overall, the experiment and analysis have correlation with fifteen out of the eighteen struts within the 10% difference threshold after additional analyses from the baseline were conducted with the objective of adding model fidelity to increase the number of struts within the threshold as discussed in Section 4.2. The additional analyses that varied the tensile and compressive elastic modulus improved correlation for two additional struts on two separate analyses; the baseline analysis using the average elastic modulus produced the best results in Table 3 resulting in 13 struts within the 10% difference threshold. There are several approaches with the experiment and the analysis that can be pursued to help improve correlation for the three remaining struts that are still over the desired error threshold.

4.4.1 Experiment Discussion

The struts with the highest error are Bottom2 and Bottom3 which both have about 25% error. Upon further investigation of the TriTruss module and instrumentation, it was noted that the strain

gages on Bottom2 and Bottom3 were positioned differently compared to Bottom1. The intention was to have the strain gages positioned on each strut as Fig. 9 illustrates, which is the way the strain gages were installed on Bottom1. The Bottom2 and Bottom3 struts had strain gages installed in the right and left positions rather than the top and bottom positions as shown in Fig. 26. A correction to ensure strain gage placement is in the appropriate orientation could improve correlation in Bottom2 and Bottom3. Since these two struts had the highest error, another solution could be to add additional strain gages on the left and right ends of each strut in the bottom triangle to capture strain the struts experience closer to the joints. In addition, LVDTs (Linear Variable Differential Transformer) and strain gages installed on the joints can help record displacements and strains that will provide additional load deflection data for correlation.

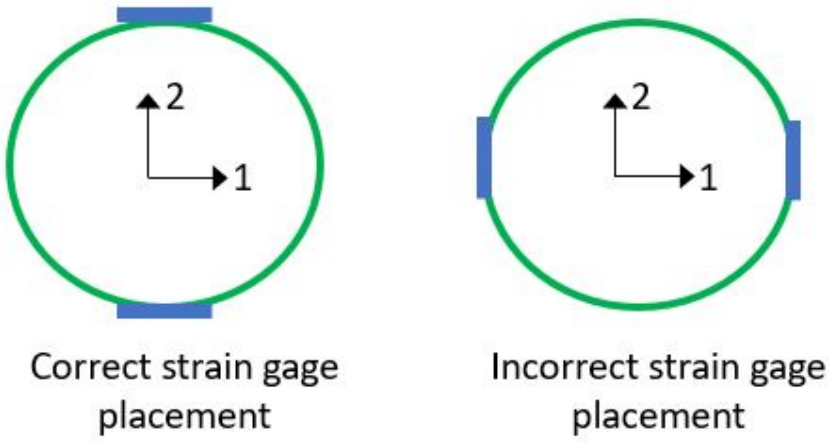

Figure 26. Configuration for strain gage application.

4.4.2 Analysis Discussion

Improvements to the FEM could be made with more detailed joint modeling. Currently, the

analysis models the joints using the approximate geometry and generic aluminum properties and assumes the struts are perfectly connected at the joints. Further testing on the joints would be needed to obtain joint properties. Also, detailed modeling of the adhesive bonding the struts to the joints could improve the accuracy of the TriTruss module model. This could also entail testing the adhesive to better model the behavior. Also, including the testing hardware of the spreader bar in the analysis could improve the results so the analysis would be more representative of the experiment. The imperfection analysis of the struts indicated that very minor imperfections significantly influence the analysis results and should be considered for all future analyses.

CHAPTER 5

CONCLUSIONS AND FUTURE WORK

The TriTruss is a novel structural module developed by researchers at NASA Langley Research Center (LaRC) that can be used in space to assemble large backing structures for a variety of applications, such as the iSAT. Since larger space telescopes require larger instruments that must meet stiffness requirements, a characterization study was needed of the TriTruss module to investigate whether it will meet the stiffness requirements. Since the TriTruss is currently at a low technology readiness level (TRL), initial testing and analysis of the structure is needed for the TriTruss to be considered in the assembly of a metering truss and primary mirror support truss for an iSAT. The purpose of this thesis was to ascertain, for the first time, the ability to measure first generation TriTruss structural response and accurately reproduce that behavior with an analytical model, establishing a framework for prediction by analysis and design tailoring. Structural characterization from testing and analysis were needed to ensure the structural performance of the struts that make up a TriTruss module. The test setup configuration and loads applied to the TriTruss module as well as the analytical methods were discussed. Also, the results obtained from tests were summarized, including a comparison with analytical results. Overall, the experiment and analysis had varying correlation with fifteen out of the eighteen struts being within the 10% error threshold. Top2, Bottom2, and Bottom3 were the only struts over the error threshold with the lowest errors resulting in 16.47%, 19.79%, and 26.31% error, respectively after further studies were conducted to improve the strut analysis correlation. There were several modifications that can be addressed to further improve the experiment and the analysis correlation. For the experiment, all strain gages

should be in the correct orientation before running future tests. Additional strain gages can also be used on the bottom struts to capture strains experienced closer to the joint, as well as including LVDTs on the joints to record any displacements that may occur. For the analysis, detailed joint modeling, including modeling of the adhesive bonding the struts, could enhance test and analysis correlation. Higher fidelity models more representative of the experiment may be able to more accurately predict the strains in the analysis. It is also important to conduct an imperfection evaluation for any struts experiencing large errors since very minor imperfections can make a significant difference in analysis results.

REFERENCES

[1] Watson, J. J., Collins, T. J., and Bush, H. G., "A history of astronaut construction of large space structures at NASA Langley Research Center," *Proceedings, IEEE Aerospace Conference*, Vol. 7, IEEE, 2002, pp. 1–19. https://doi.org/10.1109/AERO.2002.1035334.

[2] Bush, H. G., Herstrom, C. L., Heard Jr, W. L., Collins, T. J., Fichter, W., Wallsom, R. E., and Phelps, J. E., "Design and fabrication of an erectable truss for precision segmented reflector application," *Journal of Spacecraft and Rockets*, Vol. 28, No. 2, 1991, pp. 251–257.

[3] Collins, T. J., Fichter, W., Adams, R. R., and Javeed, M., "Structural Analysis and Testing of an Erectable Truss for Precision Segmented Reflector Application," NASA TP–19953518, July 1995.

[4] Lake, H. W. W. J. J. C. T. J., Mark S, "Evaluation of hardware and procedures for astronaut assembly and repair of large precision reflectors," NASA TP–2000210317, August 2000.

[5] Peacock, K., and Long, K. S., "Astronomical telescopes: a new generation." *Johns Hopkins APL Technical Digest*, Vol. 10, 1989, pp. 29–44.

[6] Doggett, W., "Robotic assembly of truss structures for space systems and future research plans," *Proceedings, IEEE Aerospace Conference*, Vol. 7, IEEE, 2002, pp. 1–10. https://doi.org/10.1109/AERO.2002.1035335.

[7] Stephens, S., and Willenberg, H. J., "Metrics for in-space telescope assembly techniques," *Proceedings, IEEE Aerospace Conference*, IEEE, 2003, pp. 1–11. https://doi.org/10.1109/AERO.2003.1235581.

[8] Lake, M. S., "Launching a 25-meter space telescope. Are astronauts a key to the next technically logical step after NGST?" *2001 IEEE Aerospace Conference Proceedings (Cat. No. 01TH8542)*, Vol. 7, IEEE, 2001, pp. 7–3611.

[9] Doggett, W. R., Dorsey, J., Teter, J., Paddock, D., Jones, T., Komendera, E. E., Bowman, L., Taylor, C., and Mikulas, M., "Persistent Assets in Zero-G and on Planetary Surfaces: Enabled by Modular Technology and Robotic Operations," *2018 AIAA SPACE and Astronautics Forum and Exposition*, American Institute of Aeronautics and Astronautics, Orlando, FL, 2018. https://doi.org/10.2514/6.2018-5305.

[10] Dorsey, J. T., "Framework for Defining and Assessing Benefits of a Modular Assembly Design Approach for Exploration Systems," *AIP Conference Proceedings*, Vol. 813, AIP, Albuquerque, New Mexico (USA), 2006, pp. 969–981. https://doi.org/10.1063/1.2169278.

[11] Belvin, W. K., Dorsey, J. T., and Watson, J. J., "Technology challenges and opportunities for very large in-space structural systems," *International Symposium on Solar Energy from Space,*, Sep. 2009.

[12] Dorsey, J., Doggett, W., Hafley, R., Komendera, E., Correll, N., and King, B., "An Efficient and Versatile Means for Assembling and Manufacturing Systems in Space," *AIAA SPACE 2012 Conference & Exposition*, AIAA Paper 2012-5115, Sep. 2012. https://doi.org/10.2514/6.2012-5115.

[13] Dorsey, J., and Watson, J., "Space Assembly of Large Structural System Architectures (SALSSA)," *AIAA SPACE 2016*, American Institute of Aeronautics and Astronautics, Long Beach, California, 2016. https://doi.org/10.2514/6.2016-5481.

[14] Belvin, W. K., Doggett, W. R., Watson, J. J., Dorsey, J. T., Warren, J. E., Jones, T. C., Komendera, E. E., Mann, T., and Bowman, L. M., "In-Space Structural Assembly: Applications and Technology," *3rd AIAA Spacecraft Structures Conference*, American Institute of Aeronautics and Astronautics, San Diego, California, USA, 2016. https://doi.org/10.2514/6.2016-2163.

[15] Thronson, H. A., Siegler, N., Polidan, R., Greenhouse, M., Grunsfeld, J., MacEwen, H., Peterson, B. M., Mukherjee, R., et al., "Future capabilities in space servicing and assembly: opportunities for future major astrophysics missions," *2018 AIAA SPACE and Astronautics Forum and Exposition, Orlando FL, September 17-19, 2018*, 2018.

[16] Doggett, W., Dorsey, J., Jones, T., Mikulas, M., Teter, J., and Paddock, D., "TriTruss: a new and novel structural concept enabling modular space telescopes and space platforms," *International Astronautical Congress*, Washington, D.C., 2019.

[17] Mukherjee, R., Siegler, N., and Thronson, H., "The Future of Space Astronomy will be Built: Results from the In-Space Astronomical Telecope (iSAT) Assembly Design Study," *International Astronautical Congress*, Washington, D.C., 2019.

[18] Siegler, N., Mukherjee, R., and Thronson, H., "NASA-Chartered in-space assembled telescope study: final report," , 2019.

[19] Cline, J., Raffanello, L. M., Song, K., White, B., McGlothin, G. S., Dorsey, J., Doggett, W. R., Mukhopadhyay, R., and Wong, I., "TriTruss Packaging and Deployment Trade Study," *ASCEND 2020*, American Institute of Aeronautics and Astronautics, Virtual Event, 2020. https://doi.org/10.2514/6.2020-4128.

[20] Simmons, L., and Song, K., "Testing of Bonds in a TriTruss Module," *AIAA SCITECH 2023 Forum*, 2023, p. 1700. https://doi.org/10.2514/6.2023-1700.

[21] Simmons, L. M., "Elastic Modulus Testing for TriTruss Sruts," NASA TM–20230011547, October 2023.

[22] Simmons, L., Song, K., and Doggett, W., "TriTruss Strut-to-Joint Bond Test: Analysis and Setup," *AIAA SCITECH 2022 Forum*, 2022, p. 0843. https://doi.org/10.2514/6.2022-0843.

[23] Smith, M., "ABAQUS/Standard User's Manual, Version 6.9," 2009. URL https://api.semanticscholar.org/CorpusID:63419830.

[24] Lake, M. S., and Georgiadis, N., "Analysis and testing of axial compression in imperfect slender truss struts," NASA TM–19904174, February 1990.

VITA

Lauren M. Simmons

Mechanical & Aerospace Engineering
Old Dominion University
214A Kaufman Hall, Norfolk, VA 23529

Education:

M.S. Mechanical Engineering, Old Dominion University, May 2024
B.S. Aerospace Engineering, Virginia Tech, May 2017